
This is an electronic reprint of the original article.
This reprint may differ from the original in pagination and typographic detail.

Vepsalainen, Antti; Paraoanu, Gheorghe Sorin
Simulating Spin Chains Using a Superconducting Circuit

Published in:
Advanced Quantum Technologies

DOI:
[10.1002/qute.201900121](https://doi.org/10.1002/qute.201900121)

Published: 01/04/2020

Document Version
Publisher's PDF, also known as Version of record

Published under the following license:
CC BY

Please cite the original version:
Vepsalainen, A., & Paraoanu, G. S. (2020). Simulating Spin Chains Using a Superconducting Circuit: Gauge Invariance, Superadiabatic Transport, and Broken Time-Reversal Symmetry. *Advanced Quantum Technologies*, 3(4), Article 1900121. <https://doi.org/10.1002/qute.201900121>

This material is protected by copyright and other intellectual property rights, and duplication or sale of all or part of any of the repository collections is not permitted, except that material may be duplicated by you for your research use or educational purposes in electronic or print form. You must obtain permission for any other use. Electronic or print copies may not be offered, whether for sale or otherwise to anyone who is not an authorised user.

Simulating Spin Chains Using a Superconducting Circuit: Gauge Invariance, Superadiabatic Transport, and Broken Time-Reversal Symmetry

Antti Vepsäläinen and Gheorghe Sorin Paraoanu*

Simulation of materials by using quantum processors is envisioned to be a major direction of development in quantum information science. Here, the mathematical analogies between a triangular spin lattice with Dzyaloshinskii–Moriya coupling on one edge and a three-level system driven by three fields in a loop configuration are exploited to emulate spin-transport effects. It is shown that the spin transport efficiency, seen in the three-level system as population transfer, is enhanced when the conditions for superadiabaticity are satisfied. It is demonstrated experimentally that phenomena characteristic to spin lattices due to gauge invariance, non-reciprocity, and broken time-reversal symmetry can be reproduced in the three-level system.

already utilized for the simulation of large spins,^[7] two-qubit dynamics,^[8] and motional averaging.^[9]

Here, we use a three-level system to simulate transport phenomena in three-spin chains with XX nearest-neighbor interaction and Dzyalozhinskii–Moriya next-nearest-neighbor interaction. These types of spin lattices play an essential role in our understanding of magnetic phenomena: they contain both the standard XX couplings and the asymmetric spin exchange found phenomenologically by Dzyaloshinskii,^[10] and whose microscopic basis, related to spin–orbit coupling and inversion symmetry breaking, has been

1. Introduction

Richard Feynman, in a landmark paper from 1982,^[1] suggested that quantum phenomena might be efficiently predicted by using other, better controllable quantum systems, as simulators. Later in 1999 Seth Lloyd showed^[2] that a universal quantum computer based on the gate model^[3] can be used to solve the Schrödinger equation by the trotterization of its unitary evolution operator. With superconducting qubits, demonstrations of such digital simulations of spin systems have been recently realized.^[4,5] While large-scale quantum computers based on the discrete gate model are still decades away, analog simulations on small-scale quantum “emulators” are presently feasible.^[6] The overhead, in terms of number of qubits and operations, is remarkably small. For example, single-device multilevel systems such as the one used in the present work have been

revealed by Moryia.^[11] These models have been studied intensively in connection with magnetic phenomena,^[12–15] see review in ref. [16]. Engineered systems that realize the same spin physics have been proposed in circuit QED^[17] and later realized experimentally.^[18,19] Related devices displaying non-reciprocity and broken time-reversal symmetry have been realized in nanomechanics^[20–23] and in degenerate ultracold gases.^[24]

We show that, in general, the spin Hamiltonian maps onto that of a multilevel system with driven transitions with complex matrix elements; thus, a multilevel system can be seen as a universal simulator of spin chains with any type of interaction. We put in evidence effects such as gauge invariance, chirality, broken-time reversal symmetry, and nonreciprocity. Our focus is on simulating transport phenomena in spin chains by a specific modulation of the couplings which will be discussed in detail below. We emphasize that also the imperfections of the real condensed-matter system (inhomogenous broadening in our case) are directly emulated by the multilevel system (through the presence of ac Stark shifts), see also the discussion in Lloyd’s seminal paper.^[2] Thus, in contrast to the case of digital simulation or quantum information processing, we do not aim at realizing high-fidelity transfer protocols; instead, we are interested in protocols that are demonstrably robust under experimental errors with realistic devices.

In general, there are two ways in which transport of excitations can be realized: sequential and adiabatic. The first implies transferring the excitation between next-neighbor sites by using Rabi pulses.^[25] The sequential method is fast but at the same time sensitive to errors in the timing of the pulses and their shape. In contrast, the adiabatic method is based on the modulation of the coupling elements in such a way that the system follows

Dr. A. Vepsäläinen, Dr. G. S. Paraoanu
QTF Centre of Excellence
Department of Applied Physics
Aalto University School of Science
P.O. Box 15100, FI-00076 Aalto, Finland
E-mail: sorin.paraoanu@aalto.fi

 The ORCID identification number(s) for the author(s) of this article can be found under <https://doi.org/10.1002/qute.201900121>

© 2020 The Authors. Published by WILEY-VCH Verlag GmbH & Co. KGaA, Weinheim. This is an open access article under the terms of the Creative Commons Attribution License, which permits use, distribution and reproduction in any medium, provided the original work is properly cited.

DOI: 10.1002/qute.201900121

the dark state, and yields the desired robustness against imperfections of the pulses. However, the method is also slow, as required by the adiabatic theorem.^[26] Several acronyms are used to describe various versions of this process.^[27] Stimulated adiabatic passage (SAP) is a general term encompassing many physical realizations: for example Bose–Einstein condensates in three wells formed by optical trapping, quantum dots, sound waves, coupled waveguides, etc. Similarly, coherent tunneling via adiabatic passage (CTAP) is often used in works on spin-1/2 particles,^[28] electrons in triple quantum dots^[29] and three-well Bose–Hubbard systems,^[30] and triangular harmonic-trap lattices where single atoms are transferred.^[31] Exactly solvable models of coherent transfer by adiabatic passage in 2D lattices, including triangular ones, were studied in ref. [32]. In the specific case of spin lattices however, spatial transport of spins is often referred to as dark-state adiabatic passage (DSAP),^[33] which is the terminology we will also use.

While both the sequential and adiabatic methods have advantages and disadvantages, there exists, surprisingly, a way to get the best of the two worlds. This is based on a simple but powerful observation made by Berry^[34] and anticipated by several authors^[35–38]: a system can follow exactly the adiabatic state by using an additional counterdiabatic Hamiltonian tailored to cancel the nonadiabatic excitations. This type of evolution is called superadiabatic or transitionless, and several variations have been explored theoretically.^[39] In spin systems, transport assisted by counterdiabatic terms has been proposed in ref. [40], a method that can be called superadiabatic DSAP (saDSAP).

In the present experiment, the goal is to simulate this form of transport by using the first three states of a superconducting transmon circuit^[41,42] by controlling the system with three microwave tones. This type of driving, called loop-drive or Δ configuration, has been discussed theoretically in various contexts in atomic physics.^[43–46] Two of the drives realize the stimulated Raman adiabatic passage (STIRAP), while the third provides the counterdiabatic correction Hamiltonian required in saDSAP. This configuration results in the creation of a synthetic gauge potential with a gauge-invariant Aharonov–Bohm phase, which can be controlled externally, allowing us to simulate the related gauge-invariance phenomenon in spin systems. This contrasts to the simpler case of two-field drive, where the phases of the driving fields can be eliminated by a gauge transformation, and also with the case of two-level systems, where again the phase of the counterdiabatic pulse is irrelevant. In three-level systems one can use this pulse sequence to realize the superadiabatic STIRAP (sa-STIRAP), provided that active time-domain compensation for ac Stark shifts is performed.^[47–49] The results present here show that it is possible to have significant population transfer also in the absence of this technique, simulating the transport in spin chains in the realistic experimental conditions when the presence of energy shifts due to magnetic fields or shifts due to modulation of the couplings.

Our results open up several interesting perspectives in circuit quantum electrodynamics, for example toward the use of driven three-level systems for realizing qubits immune to noise.^[50] The two-photon driving technique might be useful also in other systems which have a forbidden direct transition, for example in quantum optics where the Laporte rule prevents the coupling of levels with the same parity in centrosymmetric molecules.

Scaling up to chains of transmons would allow the use of the energy levels as additional synthetic dimensions and the creation of synthetic gauge potentials.^[51,52] In such configurations one could perform simulations of field theories governed by the SU(3) gauge symmetry,^[53] such as lattice QCD with its associated SU(3) color gauge. The special counterdiabatic coupling allows also for various spin-1 particle adiabatic dynamics, realizing the multilevel Cook–Shore model for spins.^[54,55] Finally, the three-level transmon can be operated with well-defined detunings, which allows the simulation of detraping phenomena in small quantum networks.^[46]

In general, superadiabatic methods form a bridge between the two paradigms of quantum control, and allow one to exploit the advantages of both. The combination of robustness under parameter fluctuations and drive errors, together with fast operation times would make superadiabatic protocols especially advantageous for reducing the effects of decoherence and increasing the signal-to-noise ratio. For adiabatic quantum computers,^[56] quantum-annealing processors,^[57,58] and holonomic quantum computing^[59–61] this would be one important route to achieving quantum advantage.^[62] In quantum thermodynamics, during the adiabatic cycle of a quantum engine the system should not only be decoupled from the thermal reservoir but also inter-level transitions should be suppressed, leading to superadiabatic engines with increased power,^[63] and providing novel insights into the foundations of the third law of thermodynamics.^[64–66] In cyclic processes, such as those used in heat engines, superadiabaticity provides a quantitative expression of Carnot’s formulation of the third law of thermodynamics by showing why absolute zero is not achievable in finite time.^[64–66] Finally, techniques of Floquet-engineering of the counterdiabatic term in Ising models^[67] and of adiabatic transfer of entanglement in quantum dot arrays^[68] and spin lattices with anti-ferromagnetic (Heisenberg) couplings,^[69] open new avenues for quantum-information tasks in complex lattices.

The paper is organized as follows: we start in Section 2 by establishing the mathematical equivalence between the single-excitation three-site spin model and the three-level transmon. We also give a straightforward derivation of the pulse sequence required for superadiabatic transport. In Section 3 we present a series of technical details on the experiment. The main results on putting in evidence the gauge-invariant phase, the broken time-reversal symmetry and the currents are presented in Section 4. Our conclusions are presented in Section 5.

2. Mapping of Spin Models into Multilevel Systems

2.1. Spin Models

Our goal is to simulate the transfer of excitation in a spin chain with a structure shown in **Figure 1**. We consider the spin Hamiltonian in a convenient parametrization,

$$H = \frac{\hbar}{4} \sum_{j \neq k} \Omega_{jk} \cos \phi_{jk} (\sigma_j^x \sigma_k^x + \sigma_j^y \sigma_k^y) + \frac{\hbar}{4} \sum_{j \neq k} \Omega_{jk} \sin \phi_{jk} (\sigma_j^x \sigma_k^y - \sigma_j^y \sigma_k^x) \quad (1)$$

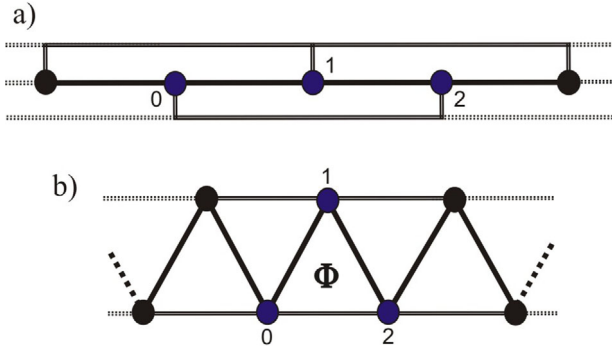


Figure 1. a) A 1D spin lattice with nearest-neighbor (single line) and next-nearest-neighbor (double line) interaction. b) Equivalent 2D representation as a triangular lattice with only nearest-neighbor interaction. In general, the interactions can be complex-valued (Peierls couplings) leading to broken-time reversal symmetry and the development of an Aharonov–Bohm gauge-invariant phase Φ . Three sites, 0, 1, 2, have been marked here (dark-blue dots), anticipating the mapping to a three-level system.

which is called the isotropic XX model with Dzyaloshinskii–Moriya interaction. The Dzyaloshinskii–Moriya term is relevant in the proximity of magnetic surfaces where spin–orbit coupling becomes relevant.

We also assume the presence of uncontrollable magnetic fields B_j on each site, leading to an additional Zeeman-splitting Hamiltonian which produces inhomogenous broadening

$$H_{\text{inh}} = -\frac{\hbar\gamma}{2} \sum_j B_j \sigma_j^z \quad (2)$$

with γ the gyromagnetic ratio. We assume that the B_j 's are fluctuating around the zero-value.

Here σ_j^x and σ_j^y are the spin-1/2 x - and y - Pauli matrices associated with the site j . Indeed, the first term is the standard XX interaction, symmetric in the exchange of x - and y and resulting from the dot product of spins, while the second results from spin–orbit interactions which has the form of a cross-product and it is anti-symmetric under the exchange of x and y . The parametrization in terms of an angle ϕ of the relative strengths of these interactions has a clear physical meaning if we write $\sigma_j^x = \sigma_j^+ + \sigma_j^-$ and $\sigma_j^y = -i\sigma_j^+ + i\sigma_j^-$, where σ_j^\pm are spin-1/2 raising and lowering operators for site j , $\sigma_j^+|\uparrow\rangle = |\downarrow\rangle$, $\sigma_j^+|\downarrow\rangle = 0$, $\sigma_j^-|\downarrow\rangle = |\uparrow\rangle$, $\sigma_j^-|\uparrow\rangle = 0$. Then

$$H = \frac{\hbar}{2} \sum_{j \neq k} \Omega_{jk} (e^{i\phi_{jk}} \sigma_j^+ \sigma_k^- + e^{-i\phi_{jk}} \sigma_j^- \sigma_k^+) \quad (3)$$

This type of Hamiltonians are relevant for the analysis of non-trivial spin structures that allow transfer of spin (angular momentum) without transfer of charge.^[70,71] The 1D lattice with nearest-neighbor and next-nearest-neighbor interactions from Figure 1a can also be seen as a 2D triangular lattice with only nearest-neighbor interactions, as shown in Figure 1b. Such lattices appear in a variety of systems—for example in Bose–Einstein condensates of atoms with two internal states in the Mott-insulator phase where it yields three-spin interactions.^[72] It was shown that spin chains with complex nearest-neighbor and next-nearest

neighbor interactions lead to the Hofstadter butterfly energy spectrum and to the appearance of edge states.^[73]

Spin transport in this model can be studied by introducing the spin current operator,^[70,71] which is obtained from the continuity equation $\partial_t \sigma_j^z + \sum_k I_{j \rightarrow k} = 0$. When comparing it to the Heisenberg equations of motion $\partial_t \sigma_j^z = \frac{i}{\hbar} [H, \sigma_j^z]$ we get

$$I_{j \rightarrow k} = i\Omega_{jk} e^{i\phi_{jk}} \sigma_j^+ \sigma_k^- - i\Omega_{jk} e^{-i\phi_{jk}} \sigma_j^- \sigma_k^+ \quad (4)$$

Also, the chirality operator in the z -direction for the triangular lattice is defined as in ref. [74]

$$C_z = \frac{1}{2\sqrt{3}} \vec{\sigma}_1 (\vec{\sigma}_2 \times \vec{\sigma}_3) \quad (5)$$

Consider the three-sites array, which will be the focus of our experiment. A very useful classification of the eigenstates of the Hamiltonian can be obtained by noticing that $[H, S_z] = 0$, where $S_z = (1/2) \sum_j \sigma_j^z$ is the total spin of the chain in the z -direction. Thus, the Hilbert space can be separated in subspaces with $S_z = -3/2, -1/2, 1/2, 3/2$, that is $|\downarrow, \downarrow, \downarrow\rangle$, $\{|\uparrow, \downarrow, \downarrow\rangle, |\downarrow, \uparrow, \downarrow\rangle, |\downarrow, \downarrow, \uparrow\rangle\}$, $\{|\downarrow, \uparrow, \uparrow\rangle, |\uparrow, \downarrow, \uparrow\rangle, |\uparrow, \uparrow, \downarrow\rangle\}$, and $|\uparrow, \uparrow, \uparrow\rangle$. In this case, the $S_z = -3/2$ and $S_z = 3/2$ states are left identical by the evolution under the Hamiltonian (1), while the dynamics on the $S_z = -1/2, 1/2$ subspaces correspond to spin waves. These waves can be also seen as the transport of a single excitation (spin-up or spin-down) in the chain.

It is important to realize that the relevant observables do not have cross-couplings between these subspaces. The operator that counts the number of spin excitations, $N = \sum_j \sigma_j^+ \sigma_j^-$ has eigenvalues 0, 1, 2, and 3 on these subspaces since $N = 3/2 + S_z$. The currents also have zero matrix elements between subspaces with different S_z . For the chirality, the eigenvectors $|C_z, S_z\rangle$ in the subspace $S_z = -1/2$ are

$$|C_z, -1/2\rangle = \frac{1}{\sqrt{3}} (|\uparrow\downarrow\downarrow\rangle + e^{2iC_z\pi/3} |\downarrow\uparrow\downarrow\rangle + e^{4iC_z\pi/3} |\downarrow\downarrow\uparrow\rangle), \quad (6)$$

with eigenvalues $C_z = 0, \pm 1$. The eigenvalues of C_z on the $S_z = 1/2$ subspace are obtained by flipping all the spins,

$$|C_z, 1/2\rangle = \sigma_1^x \sigma_2^x \sigma_3^x |C_z, -1/2\rangle. \quad (7)$$

2.2. Multilevel Hamiltonians

To simulate the dynamics of the Hamiltonian Equation (1), the key observation is that the number of spin excitations is conserved by the dynamics. Thus, the $2^3 = 8$ -dimensional Hilbert space breaks down into two 3D Hilbert spaces and two other additional states with no dynamics. Due to this property the simulation can be realized using a three-level system with states $|0\rangle$, $|1\rangle$, and $|2\rangle$.

Consider for example the subspace $S_z = -1/2$ ($N = 1$). We can identify $|\uparrow, \downarrow, \downarrow\rangle = (1, 0, 0)^T = |0\rangle$, $|\downarrow, \uparrow, \downarrow\rangle = (0, 1, 0)^T = |1\rangle$, $|\downarrow, \downarrow, \uparrow\rangle = (0, 0, 1)^T = |2\rangle$. Similarly, for $S_z = 1/2$ ($N = 2$) we identify $|\downarrow, \uparrow, \uparrow\rangle = (1, 0, 0)^T = |0\rangle$, $|\uparrow, \downarrow, \uparrow\rangle = (0, 1, 0)^T = |1\rangle$, $|\uparrow, \uparrow, \downarrow\rangle = (0, 0, 1)^T = |2\rangle$.

Inhomogenous-broadening terms appear in the simulator mostly as a result of ac Stark shifts, which can be significant if the values of the amplitudes of the pulses are large. We therefore have

$$H_{\text{acStark}} = \frac{\hbar}{2} \sum_j \epsilon_j |j\rangle\langle j|, \quad (8)$$

which reproduces the action of H_{inh} with $\epsilon_j = \pm\gamma(\sum_{k \neq j} B_k - B_j)$ on the subspaces with $S_z = \pm 1/2$.

The operators appearing in Equation (1) can be identified with the Gell–Mann operators (see Section 1A, Supporting Information).

$$\Lambda_{jk}^s \leftrightarrow \sigma_j^+ \sigma_k^- + \sigma_j^- \sigma_k^+ = \frac{1}{2} (\sigma_j^x \sigma_k^x + \sigma_j^y \sigma_k^y) \quad (9)$$

$$\Lambda_{jk}^a \leftrightarrow -i\sigma_j^+ \sigma_k^- + i\sigma_j^- \sigma_k^+ = -\frac{1}{2} (\sigma_j^x \sigma_k^y - \sigma_j^y \sigma_k^x) \quad (10)$$

Here Λ_{jk}^s and Λ_{jk}^a are the symmetric and antisymmetric Gell–Mann operators defined as: $\Lambda_{jk}^s = \Lambda_{kj}^s = |j\rangle\langle k| + |k\rangle\langle j|$ (symmetric) and $\Lambda_{jk}^a = -\Lambda_{kj}^a = -i|j\rangle\langle k| + i|k\rangle\langle j|$ (anti-symmetric).

As we will see, the Hamiltonian

$$H = \frac{\hbar}{2} \Omega_{01} \hat{\mathbf{n}}_{01} \cdot \mathbf{\Lambda}_{01} + \frac{\hbar}{2} \Omega_{12} \hat{\mathbf{n}}_{12} \cdot \mathbf{\Lambda}_{12} + \frac{\hbar}{2} \Omega_{02} \hat{\mathbf{n}}_{02} \cdot \mathbf{\Lambda}_{02} \quad (11)$$

can be implemented by driving a transmon qubit in the loop configuration with Rabi frequencies $\Omega_{jk} = \Omega_{kj}$, and with ϕ_{jk} the phases of the driving fields where by convention $\phi_{jk} = -\phi_{kj}$, where $\hat{\mathbf{n}}_{jk}$ are unit vectors in a plane defined as $\hat{\mathbf{n}}_{jk} = (\cos \phi_{jk}, -\sin \phi_{jk})$, with $j, k \in \{0, 1, 2\}$. The matrix vector comprising the Gell–Mann matrices is defined as $\Lambda_{jk} = (\Lambda_{jk}^s, \Lambda_{jk}^a)$.

This Hamiltonian realizes the so-called loop driving configuration for three-level systems^[44,45] (also referred to as Δ configuration^[46]) with complex (Peierls) couplings between each pair of states.

In the simulator, the currents can be obtained from identifying the population on a level j with the operator $\frac{1}{2}(1 + \sigma_z)$ for the case $S_z = -1/2$ ($N = 1$) and with $\frac{1}{2}(1 - \sigma_z)$ for the case $S_z = 1/2$ ($N = 2$). Indeed, when averaged on superpositions of $\{|\uparrow, \downarrow, \downarrow\rangle, |\downarrow, \uparrow, \downarrow\rangle, |\downarrow, \downarrow, \uparrow\rangle\}$ these operators yield the modulus squared of the complex amplitude of the state with the j spin flipped. Thus, the currents in the simulator are

$$I_{j \rightarrow k} = -\frac{\Omega_{jk}}{2} (\sin \phi_{jk} \Lambda_{jk}^s - \cos \phi_{jk} \Lambda_{jk}^a) \quad (12)$$

The chiral operator corresponding to Equation (5) can be identified straightforwardly as

$$C_z = \frac{\sqrt{3}}{3} (\Lambda_{01}^a + \Lambda_{12}^a + \Lambda_{20}^a) \quad (13)$$

Chiral states are obtained as a quantum Fourier transform

$$|C_z\rangle = \frac{1}{\sqrt{3}} \sum_{j=0,1,2} e^{2\pi i j C_z / 3} |j\rangle \quad (14)$$

Table 1. Summary of equivalence between the spin chain and the simulator.

Spin chain	Simulator
$N = 1$ or $N = 2$ subspaces of three spins	qutrit Hilbert space
XX interaction	Λ^z coupling
Dzyaloshinskii–Moriya interaction	Λ^a coupling
inhomogeneous broadening	ac Stark shifts
chirality	quantum Fourier
DSAP	STIRAP
saDSAP	saSTIRAP

which can be immediately inverted

$$|j\rangle = \frac{1}{\sqrt{3}} \sum_{j=0,1,2} e^{-2\pi i j C_z / 3} |C_z\rangle \quad (15)$$

2.3. Adiabatic and Superadiabatic Processes

The possibility of manipulation of the couplings of the spin chain raises the issue of efficient and robust transfer of state between sites. This can be done by employing adiabatic and superadiabatic processes.

For both the spin chain and the multilevel simulator we can define the DSAP and respectively the STIRAP processes by the requirement that the system follows the dark state $|D(t)\rangle = \cos \Theta(t)|0\rangle - \sin \Theta(t)|2\rangle$, as the mixing angle $\Theta(t) = \tan^{-1}[\Omega_{01}(t)/\Omega_{12}(t)]$ is varied slowly from 0 to $\pi/2$. Let us recall that the eigenvalues of the STIRAP Hamiltonian $H_{01}(t) + H_{12}(t)$ comprise the dark state $|D(t)\rangle$ with eigenvalue 0, as well as two states of the form $(\sin \Theta|0\rangle + \cos \Theta|2\rangle \pm |1\rangle)/\sqrt{2}$ with eigenvalues $\pm \hbar \sqrt{\Omega_{01}^2 + \Omega_{12}^2}/2$, respectively, see for example ref. [85]. Here $\sin \Theta|0\rangle + \cos \Theta|2\rangle$ is the bright state, orthogonal to the dark state in the subspace $\{|0\rangle, |2\rangle\}$.

To accelerate the process, one could use the concept of superadiabaticity, where a counterdiabatic correction pulse is applied to suppress excitations on states other than the dark state. The resulting protocols are denoted by saSTIRAP for the simulator and saDSAP for the spin chain. **Table 1** summarizes the equivalence between the two systems. The form of the counterdiabatic pulse in the case of three-level systems can be found by applying the general superadiabatic protocol^[34,36–38] to the case of STIRAP.^[75,76] It is interesting to note that in this specific case, the counterdiabatic Hamiltonian was found^[44,45] several years before the general formalism^[34,36–38] was developed. In Section 1C, Supporting Information, we provide a proof of these results based on the method of adiabatic potentials.^[77] Here we give a direct, straightforward derivation based on the Schrödinger equation.

Specifically, we would like to find under which conditions the dark state is a solution of the Schrödinger equation with total Hamiltonian $H_{01}(t) + H_{12}(t) + H_{02}(t)$. This leads immediately to

$$\sin \Theta (2i\dot{\Theta} - e^{-i\Phi} \Omega_{02}) |0\rangle + \cos \Theta (2i\dot{\Theta} + e^{i\Phi} \Omega_{02}) |2\rangle = 0 \quad (16)$$

where $\Phi = \phi_{01} + \phi_{12} + \phi_{20}$ is the gauge-invariant phase, to be discussed in detail later. We see that this can be satisfied only

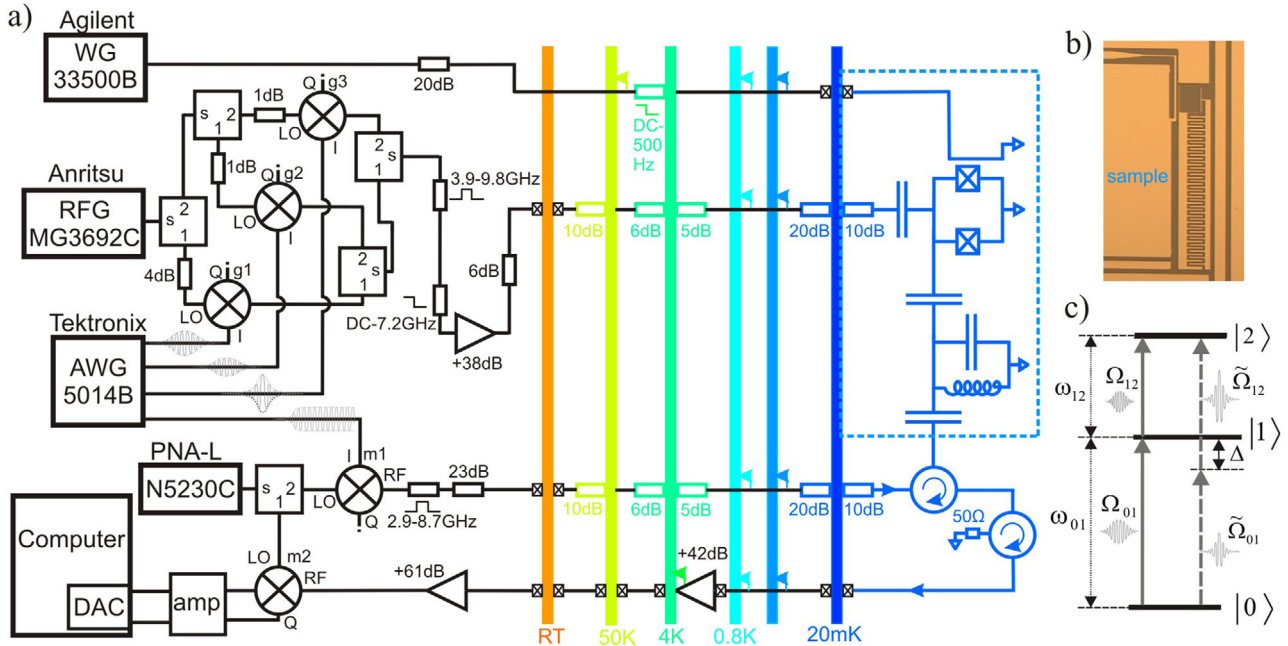


Figure 2. Schematic of the experimental platform used for simulations. a) Microwave instruments and components at various temperature stages are used to control the transmon device installed at the mixing chamber. b) Optical image of the sample, showing the transmon and part of the coplanar waveguide resonator used for measurement. c) Energy levels and driving fields in the loop driving configuration. STIRAP pulses $\Omega_{01}(t)$ and $\Omega_{02}(t)$ are applied resonantly into the transitions $\omega_{01}(t)$ and $\omega_{02}(t)$, respectively, while the counteradiabatic control is realized by the two pulses $\tilde{\Omega}_{01}$ and $\tilde{\Omega}_{12}$ with detuning Δ .

if $\Phi = -\pi/2$ and $\Omega_{02} = 2\dot{\Theta}(t)$. Thus, if we set $\phi_{01} = \phi_{12} = 0$, the counteradiabatic Hamiltonian takes the form

$$H_{cd}(t) = -\frac{\hbar}{2}\Omega_{02}(t)\Lambda_{02}^a = \frac{\hbar}{2}\Omega_{02}(t)\Lambda_{20}^a \quad (17)$$

where, as previously, $\Lambda_{kl}^a = -\Lambda_{lk}^a = -i|k\rangle\langle l| + i|l\rangle\langle k|$ are the anti-symmetric Gell–Mann matrices.

It is interesting to note that the Gell–Mann matrices $\Lambda_{01}^s, \Lambda_{12}^s$, and Λ_{02}^a , form a closed subalgebra and can be regarded respectively as the x, y , and z -components of a spin-1 particle since $[\Lambda_{01}^s, \Lambda_{12}^s] = i\Lambda_{02}^a$ and circular permutations thereof. Thus, STIRAP can be seen as the adiabatic guiding of a spin-1 in the xOy plane by a magnetic field with x, y -components $(\Omega_{01}, \Omega_{12})$. The mixing angle Θ is then the angle formed by the magnetic field (and the spin which follows its direction) with the y -axis. Interestingly, saSTIRAP achieves a faster motion in the same plane by adding a control field in the z -direction: the corresponding spin z -component produces a rotation in the $x - y$ plane designed such that it cancels exactly the nonadiabatic terms.

3. Experimental Platform

3.1. Measurement and Control Setup

Our experiments run on a superconducting-circuit platform, as shown in Figure 2a. As a multilevel simulator we use a transmon device,^[41] which consists of a Cooper pair box with large shunting capacitors inserted in the gap between the signal line and the

ground of a coplanar waveguide. The latter is configured as a $\lambda/4$ resonator and used for dispersive readout. The bare resonance frequency of the resonator (measured with the qubit far-detuned) is $f_r \simeq 5.13$ GHz, and for the quality factor we obtain $Q \simeq 7000$. The size of the Josephson junctions is 150×170 nm² and it is fabricated from aluminum (90 nm film thickness) by shadow angle evaporation on a high-resistivity Si substrate; the chip is bonded and installed in a dilution refrigerator with ~ 20 mK base temperature (Figure 2b). The device is biased by a magnetic field applied by using an additional line which is shortcut to the ground in the proximity of the SQUID loop of the device. For this, at room temperature we use an Agilent 33500B waveform generator, while a passive low pass RC-filter anchored to the 4K-flange of the refrigerator (cutoff frequency of ~ 500 Hz) is used to filter out the thermal noise.

The transmon is controlled by sending microwave pulses through a coplanar waveguide which is evaporated on the chip and capacitively interacts with the large transmon shunting capacitor. The pulses are created by mixing their envelopes, created by an arbitrary waveform generator (Tektronix 5014B), with a continuous microwave tone. In the setup, three IQ-mixers (IQ-0307L), denoted by g_1, g_2 , and g_3 , are used to create pulses at three different control frequencies (Figure 2a). In order to ensure the phase-coherence of the pulses, a single local oscillator tone at 7.608 GHz (generated by an Anritsu MG3692C) is used, and the pulse envelopes are digitally modulated by an intermediate frequency tone.

The mixers are calibrated at the beginning of each experiment by standard techniques in order to reduce the leakage and the spurious sidebands. The detection scheme is a homodyne

measurement: the signal from a vector network analyzer (PNA-L N5230C) at a frequency $f_p = 5.1249$ GHz is split into two parts, one mixed in the IQ-mixer m1 (IQ-0307LXP) with a rectangular waveform, and the other used as the LO. Demodulation and digitization is done by mixer m2 (IQ-0307LXP) and by an analog-to-digital converter (Acqiris U1082a). To perform quantum state tomography, we record the demodulated traces in time domain. We first prepare the system in the states $|0\rangle$, $|1\rangle$, and $|2\rangle$ and use these traces as calibration. The calibration measurement fidelities of the states $|1\rangle$ and $|2\rangle$, with $|0\rangle$ as reference, are 95.7% and 88.4%, respectively. To extract the populations for a general state, we assume the measured trace to be a linear combination of the calibration traces. Using the least squares fit, we can extract the coefficients of the linear combination in the basis of the calibration traces.^[78]

We first characterize the device: spectroscopy measurements allow us to identify the transition frequencies ω_{01} and ω_{12} between the energy levels of the device at different bias magnetic fields and extract the parameters of the electrical circuit. We obtain a Josephson energy at the sweet spot $E_{J\bar{z}} = E_{J,1} + E_{J,2} \simeq h \times 26.235$ GHz, a charging energy $E_C \simeq h \times 282$ MHz (which results in an anharmonicity $\hbar\omega_{12} - \hbar\omega_{01} \approx -E_C$), and a junction asymmetry $d = |E_{J,1} - E_{J,2}|/(E_{J,1} + E_{J,2}) \simeq 0.02$. When the qubit frequency is tuned to be on resonance with the $\lambda/4$ resonator, we observe an avoided crossing in the spectrum, which allows us to extract the qubit-resonator coupling $g \simeq 103$ MHz. After this, the magnetic field is kept fixed at a bias point corresponding to $\omega_{01}/(2\pi) = 7.381$ GHz and $\omega_{12}/(2\pi) = 7.099$ GHz.

At this biasing point, we measure the relaxation rates from the state 1 and 2 by exciting the system with π pulses and recording the decay. We obtain $\Gamma_{10} = 5.0$ MHz and $\Gamma_{21} = 7.0$ MHz. From Ramsey interference experiments, we find that in this sample the dephasing times are dominated by the energy relaxation. To model the decoherence, we use the standard Lindblad formalism for a three-level system,^[79,80] with a superoperator $\mathcal{L}[\rho] = -\Gamma_{21}\rho_{22}|2\rangle\langle 2| - (\Gamma_{10}\rho_{11} - \Gamma_{21}\rho_{22})|1\rangle\langle 1| + \Gamma_{10}\rho_{11}|0\rangle\langle 0|$.

3.1.1. STIRAP pulses

In order to create the microwave pulses used for STIRAP, we apply two IF waves with Gaussian envelopes $\exp[-\frac{t^2}{2\sigma^2}]$, $\exp[-\frac{(t-t_s)^2}{2\sigma^2}]$ and phases ϕ_{01} , ϕ_{12} to the I ports of the mixers g1 and g2. These pulses couple resonantly into the $0 \leftrightarrow 1$ and $1 \leftrightarrow 2$ transitions, resulting in Rabi couplings

$$\Omega_{01}(t) = \Omega_{01} \exp\left[-\frac{t^2}{2\sigma^2}\right] \quad (18)$$

$$\Omega_{12}(t) = \Omega_{12} \exp\left[-\frac{(t-t_s)^2}{2\sigma^2}\right] \quad (19)$$

and yielding the matrix elements $\langle 0|H(t)|1\rangle = \langle 1|H(t)|0\rangle^* = \Omega_{01}(t) \exp(i\phi_{01})$ and $\langle 1|H(t)|2\rangle = \langle 2|H(t)|1\rangle^* = \Omega_{12}(t) \exp(i\phi_{12})$. For convenience, the Gaussians were truncated at $\pm 3\sigma$. The Gaussian pulses are not the only possible choice for the STIRAP pulse shape, but they are experimentally and theoretically convenient without sacrificing performance.^[76] In this parametrization

σ is the width of the pulses, and the counterintuitive STIRAP sequence is realized at negative pulse separation times $t_s < 0$. The resulting form of the STIRAP Hamiltonian^[81] in the Gell–Mann representation is then

$$H_{\text{STIRAP}}(t) = \frac{\hbar}{2}\Omega_{01}(t)\hat{\mathbf{n}}_{01} \cdot \mathbf{\Lambda}_{01} + \frac{\hbar}{2}\Omega_{12}(t)\hat{\mathbf{n}}_{12} \cdot \mathbf{\Lambda}_{12} \quad (20)$$

which reproduces the first two terms of Equation (11).

3.1.2. Counterdiabatic drive

If the adiabaticity condition for STIRAP is broken, for example by attempting to drive the system too fast, the system gets diabatically excited away from the state $|D(t)\rangle$, reducing the transferred population. However, it is possible to accelerate the STIRAP protocol by employing the technique of reverse Hamiltonian engineering.^[34,36–38] This requires the addition of a counterdiabatic pulse with a very specific shape and with complex coupling into the $0 - 2$ transition - which for the case of transmon is a forbidden transition in the first order. To create this pulse, we generate an IF signal with envelope $\cosh^{-1/2}[t_s(t - t_s/2)/\sigma^2]$ and phase $\tilde{\varphi}$, and apply it to the I port of the mixer g3. The frequency of the IF tone is set such that, after mixing with the local oscillator, the resulting upconverted frequency would match half of the forbidden transition $\omega_{02}/(2\pi) = 14.480$ GHz. Thus, this two-photon drive is detuned from both the $0 - 1$ and $1 - 2$ transitions by an amount $\pm\Delta$, which equals to half the transmon anharmonicity $\Delta = (\omega_{01} - \omega_{12})/(4\pi) = 141$ MHz. This generates an effective matrix element $\langle 0|H(t)|2\rangle = \langle 2|H(t)|0\rangle^* = \Omega_{02}(t) \exp(i\phi_{02})$ without populating the state $|1\rangle$. The Rabi coupling $\Omega_{02}(t)$ is obtained from the perturbation theory^[82] as $\Omega_{02}(t) = \tilde{\Omega}_{01}(t)\tilde{\Omega}_{12}(t)/(2\Delta)$ and $\phi_{02} = -\phi_{20} = 2\tilde{\varphi} + \pi$. Note that we define Ω_{02} as a real positive quantity. Thus we obtain the last term from Equation (11)

$$H_{02}(t) = \frac{\hbar}{2}\Omega_{02}(t)\hat{\mathbf{n}}_{02} \cdot \mathbf{\Lambda}_{02} \quad (21)$$

Satisfying the relation $\Phi = \phi_{01} + \phi_{12} + \phi_{20} = -\pi/2$ amounts to producing a complex Peierls matrix element $\langle 0|H_{\text{cd}}(t)|2\rangle = \langle 2|H_{\text{cd}}(t)|0\rangle^* = (\hbar/2)\Omega_{02}(t) \exp(i\pi/2)$. For equal-amplitude Gaussian STIRAP pulses, from the relation $\Omega_{02}(t) = 2\tilde{\Theta}(t)$ we get $\Omega_{02}(t) = -(t_s/\sigma^2) \cosh^{-1}[t_s(t - t_s/2)/\sigma^2]$.

3.2. Pulse Calibration

Overall, the pulses described above results in couplings of the form $H(t) = \sum_{j \neq k} H_{jk}(t)$, where $H_{jk}(t) = \frac{\hbar}{2}\Omega_{jk}(t)(\cos \phi_{jk}\Lambda_{jk}^s - \sin \phi_{jk}\Lambda_{jk}^a)$, which reproduces the form Equation (11). In addition to these terms, ac Stark shifts are produced by off-resonant drives. In our case, the largest ac Stark shifts are produced by the two-photon pulse, which effectively displaces the energy levels of the qutrit as seen by the STIRAP pulses; this produces in general (see Section 2, Supporting Information) $H_{\text{acStark}}(t) = \frac{\hbar}{2} \sum_j \epsilon_j(t)|j\rangle\langle j|$ as in Equation (8). These shifts are expected to occur also in the spin chain, where they will appear as inhomogenous broadening. In principle it is possible to exactly cancel these shifts by techniques

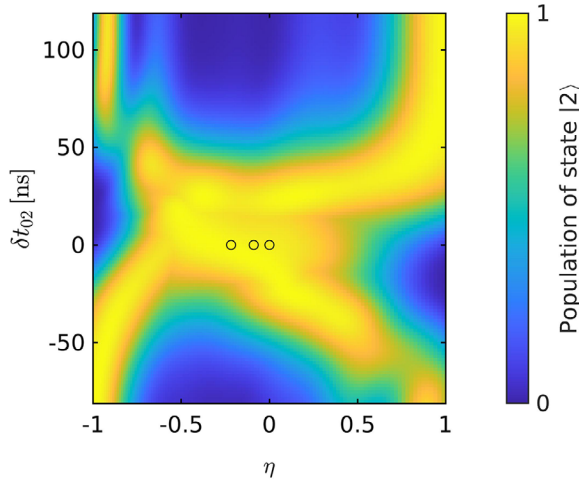


Figure 3. The population of the state $|2\rangle$ as a function of the amplitude pulse asymmetry $\eta = (\Omega_{12} - \Omega_{01})/(\Omega_{12} + \Omega_{01})$ of the STIRAP pulses and of the time shifts of the counterdiabatic pulse $\Omega_{02}(t) \rightarrow \Omega_{02}(t - \delta t_{02})$. The black circles correspond to the values used in experiments, $\eta = -0.22, -0.09$, and a reference $\eta = 0$, from left to right. The parameters used in the numerics are $k = |t_s|/\sigma = 2.45$ and $\sigma = 25$ ns.

such as time-dependent frequency corrections^[47–49] or by an additional two-photon drive, designed with a detuning with opposite sign and a π phase in one of the drives.^[50] However, whether these techniques can be implemented depends on the particular physical system and the associated array of available experimental methods. For example, in optical systems the control of the phase of the lasers might not be possible with sufficient accuracy.

Here, we attempt to optimize the transfer by varying the parameters of the STIRAP pulses and the timing of the counterdiabatic pulse. The results are presented in **Figure 3**. Note that for the numerics we use the full Hamiltonian $\mathcal{H} = \mathcal{H}_{01} + \mathcal{H}_{12} + \mathcal{H}_{02}$ as given in Section 1B [Equations (1), (2), and (7)], Supporting Information, which incorporates all cross-couplings of the fields into the transmon transitions. We characterize the pulse amplitude asymmetry of the Gaussian pulses by a parameter $\eta = (\Omega_{12} - \Omega_{01})/(\Omega_{12} + \Omega_{01})$ and we shift the counterdiabatic pulses by a quantity δt_{02} , $\Omega_{02}(t) \rightarrow \Omega_{02}(t - \delta t_{02})$. From **Figure 3** we observe the existence of a rather large plateau of transferred population around $\delta t_{02} = 0$, showing a quite remarkable insensitivity to the STIRAP pulse symmetry. For the experiments, we choose to operate at two points, ($\eta = -0.22$, $\delta t_{02} = 0$) and ($\eta = -0.09$, $\delta t_{02} = 0$) which are somewhat in the middle of one of the plateaus and therefore are less exposed to errors. Using these pulses we typically reach experimental values for p_2 in the range $0.8 - 0.9$.

4. Results

4.1. Synthetic Gauge-Invariant Phase

The calibration procedure described above was done by optimizing one of the phases of the three pulses while keeping the other two fixed. This is allowed by the gauge-invariance of the system with respect to the total circular phase $\Phi = \phi_{01} + \phi_{12} + \phi_{20}$ as we will demonstrate explicitly here.

To show this, we first examine the coupling Hamiltonian Equation (11)

$$H(t) = \frac{\hbar}{2} \Omega_{01}(t) \hat{\mathbf{n}}_{01} \cdot \mathbf{\Lambda}_{01} + \frac{\hbar}{2} \Omega_{12}(t) \hat{\mathbf{n}}_{12} \cdot \mathbf{\Lambda}_{12} + \frac{\hbar}{2} \Omega_{02}(t) \hat{\mathbf{n}}_{02} \cdot \mathbf{\Lambda}_{02}, \quad (22)$$

comprising the driving fields that couple into each pair of states $k, l \in \{0, 1, 2\}$ with Rabi frequencies Ω_{jk} (real and positive) and phases ϕ_{jk} . This describes three simultaneous rotations in the three subspaces $0 - 1$, $1 - 2$, and $0 - 2$ around the vectors $\hat{\mathbf{n}}_{kl}$. In each of the subspaces (k, l) , the action of the Hamiltonian is analogous to that of a spin-1/2 particle in a magnetic field of magnitude Ω_{12} and direction $\hat{\mathbf{n}}_{kl}$. For a single spin-1/2 particle it is always possible to rotate the axis so that one of them overlaps with the direction of the magnetic field. Crucially, for the three-level system it is not possible to rotate arbitrarily all the three vectors $\hat{\mathbf{n}}_{kl}$. Indeed, by applying a unitary $U = e^{-i\chi_0}|0\rangle\langle 0| + e^{-i\chi_1}|1\rangle\langle 1| + e^{-i\chi_2}|2\rangle\langle 2|$ one obtains a Hamiltonian UHU^\dagger with a similar structure as Equation (11) but with different angles ϕ'_{kl} ; these new angles are not arbitrary, but they satisfy the constraint $\phi'_{01} + \phi'_{12} + \phi'_{20} = \phi_{01} + \phi_{12} + \phi_{20} = \Phi$. By performing local gauge transformations we can always eliminate two of the phases but the third one will be constrained by the value of the gauge-invariant quantity Φ . The situation is mathematically similar with that of a three-site system with complex hopping elements (Peierls hopping)^[83] and a magnetic field piercing the plaquette and creating a flux Φ .^[51,52] This conclusion holds also for the total Hamiltonian $H + H_{\text{acStark}}$, since by inspecting the ac Stark part Equation (8)

$$H_{\text{acStark}}(t) = \frac{\hbar}{2} \sum_j \epsilon_j(t) |j\rangle\langle j| \quad (23)$$

we have $UH_{\text{acStark}}U^\dagger = H_{\text{acStark}}$. We can then define the Wilson loop around the triangle contour as

$$W_\Delta = e^{i\phi_{01} + \phi_{12} + \phi_{20}} = e^{i\Phi} \quad (24)$$

which is the path-ordered product of link variables $\exp(i\phi_{jk}) \in U(1)$.

In **Figure 4** we present the population transferred to state $|2\rangle$ using saSTIRAP when either of the angles ϕ_{01} , ϕ_{12} , and $\tilde{\varphi}$ are varied, while keeping the other two fixed. The populations are measured at a time $t = 20$ ns. The experiment shows clearly that the method can successfully transfer population to state $|2\rangle$, given the correct choice of the phases and shows that the three phases for a given transferred population are not independent from each other. From the data, the π -periodicity of the population transferred as a function of the phase $\tilde{\varphi}$ of the two-photon drive pulse is also manifest. In contradistinction, a sequential process (where we populate the first excited state, then transfer to the second excited state) should display a 2π periodicity in the single-photon drive phase. This demonstrates the fully quantum-coherent nature of the process.

Once the phenomenon of gauge invariance is demonstrated, we can proceed by fixing the gauge. A convenient choice is

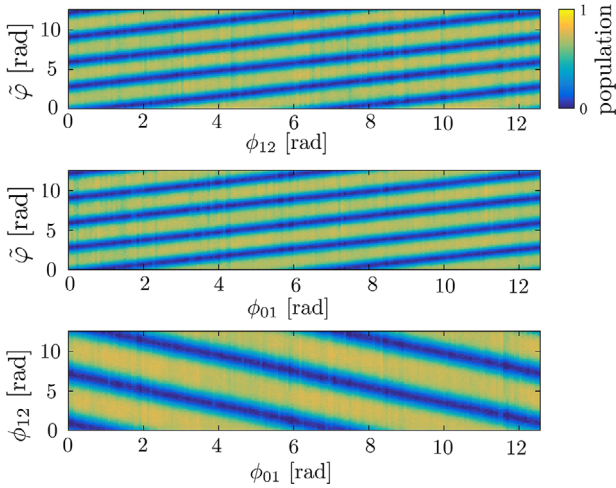


Figure 4. Transferred population p_2 as a function of the phases ϕ_{01} , ϕ_{12} , and $\tilde{\varphi}$ of the externally applied microwave fields. The three plots correspond, from the upper to the lower picture, to $\phi_{01} = 0$, $\phi_{12} = 0$ and $\tilde{\varphi} = 0$, respectively; the other parameters for these measurements are $\Omega_{01}/(2\pi) = 25$ MHz, $\Omega_{12}/(2\pi) = 16$ MHz ($\eta = -0.22$), $t_s = -45$ ns, and $\sigma = 30$ ns. The slope of the constant-population lines are positive in the two upper pictures and negative in the lowest one, and the $\tilde{\varphi}$ periodicity is twice as large as that of the periodicity in ϕ_{01} and ϕ_{12} . This verifies the relation $\phi_{01} + \phi_{12} - 2\tilde{\varphi} - \pi = \Phi$.

$\phi'_{01} = 0$, $\phi'_{12} = 0$, and $\phi'_{20} = \Phi$, which leads to the following structure for Equation (11),

$$H_{\Phi}(t) = \frac{\hbar}{2}\Omega_{01}(t)\Lambda_{01}^s + \frac{\hbar}{2}\Omega_{12}(t)\Lambda_{12}^s + \frac{\hbar}{2}\Omega_{02}(t)\hat{n}_{\Phi} \cdot \Lambda_{02}, \quad (25)$$

where $\hat{n}_{\Phi} = (\cos \Phi, \sin \Phi)$. This form puts in evidence the role of the gauge-invariant phase Φ as a parameter in the Hamiltonian, which can be controlled experimentally along with the Rabi frequencies $\Omega_{01}(t)$, $\Omega_{12}(t)$, and $\Omega_{02}(t)$.

4.2. Broken Time-Reversal Symmetry

For a spin lattice the time-reversal symmetry is relatively straightforward to understand. A magnetic field, either applied externally or resulting from the complex phases of the couplings, remains invariant when time runs backward; as a result, the time-reversed Schrödinger equation is no longer satisfied. This leads to nonreciprocal phenomena: an input signal at one lattice site might be transmitted to another site, but nothing will be transmitted if we reverse the direction of the signal. In practice, this can be used for realizing non-reciprocal devices such as circulators or isolators.

Here, we examine in detail the time-reversal symmetry of the problem. We first note that STIRAP itself is clearly time-symmetric. Indeed, starting from state $|2\rangle$ as the initial state and running backward in time the STIRAP process, the system will see the Ω_{01} wave as the Stokes pulse and then the Ω_{12} wave as the pump pulse, thus realizing the usual counterintuitive sequence. Experimentally, STIRAP reversal has been demonstrated already in ref. [81]. This can be understood by recalling that in this situation the wavefunction simply follows the slow variation of the Hamiltonian dark state as the mixing angle varies from 0 to $\pi/2$. Thus, when reversing the direction of time, $\Theta \rightarrow \pi/2 - \Theta$

and $\cos \Theta|0\rangle - \sin \Theta|2\rangle \rightarrow -(\cos \Theta|2\rangle - \sin \Theta|0\rangle)$, with the roles of the states $|2\rangle$ and $|0\rangle$ reversed, as expected.

The situation changes dramatically when the additional transfer path provided by the two-photon pulse is introduced and the gauge-invariant phase Φ is established. In the spin system one sees immediately that this is equivalent to the appearance of a magnetic field piercing the plaquette. We do expect then to have a broken time symmetry if this magnetic field is non-zero, and a time-symmetric problem otherwise, and similar considerations will hold for the three-level system.

As usual in time-reversal problems, we define an antilinear complex conjugation operator \mathcal{K} ; when applied from the right to the Schrödinger equation

$$i\hbar \frac{\partial |\psi(t)\rangle}{\partial t} = H_{\Phi}(t)|\psi(t)\rangle \quad (26)$$

we obtain

$$-i\hbar \frac{\partial \mathcal{K}|\psi(t)\rangle}{\partial t} = \mathcal{K}H_{\Phi}(t)\mathcal{K}\mathcal{K}|\psi(t)\rangle \quad (27)$$

where we used $\mathcal{K}^2 = 1$. A time-reversed Schrödinger equation

$$i\hbar \frac{\partial |\psi'(t')\rangle}{\partial t'} = H'_{\Phi'}(t')|\psi'(t')\rangle, \quad (28)$$

where $t' = -t$, can be obtained by identifying $|\psi'(t')\rangle = \mathcal{K}|\psi(t)\rangle$ and $H'_{\Phi'}(t') = \mathcal{K}H_{\Phi}(t)\mathcal{K}$. By examining Equation (25) we notice that $\mathcal{K}H_{\Phi}(t)\mathcal{K} = H_{-\Phi+2n\pi}(t)$. Thus, the time-reversed evolution corresponds to changing the gauge-invariant phase to $\Phi' = -\Phi + 2n\pi$ (or $\tilde{\varphi}' = -\tilde{\varphi} - (n+1)\pi$), and the time-reversal symmetry is broken for all values of Φ , with the exception of $\Phi = n\pi$ (or $\tilde{\varphi} = -(n+1)\pi/2$). These results agree also with the findings in ref. [17] for a three-site lattice, corresponding to reversing the direction of magnetic field piercing the lattice in Figure 1b. It is important to understand that these considerations do not depend on the particular gauge used in Equation (25); the same conclusion is reached if the Hamiltonian Equation (11) is examined. This is due to the fact that no gauge transformation can make the Hamiltonian Equation (11) real, with the exception of the case $\Phi = \phi_{01} + \phi_{12} + \phi_{20} = n\pi$. In the spin lattice, this case corresponds to an integer number of flux quanta per unit cell. Also, because the Hamiltonian H_{acStark} is invariant under time-reversal (there is no phase-dependence in the ac Stark shifts), the breaking of the time-reversal symmetry due to H_{Φ} should be observable when the system is evolved under the full Hamiltonian comprising also the inhomogenous/ac-Shifted part.

To demonstrate the gradual onset of the broken time-symmetry regime, we perform the experiments shown in Figure 5, where we measure the transferred populations at different phases $\tilde{\varphi}$. We introduce the area of the counterdiabatic pulse $\mathcal{A}_{02} = \int_{-\infty}^{\infty} dt \Omega_{02}(t)$ and we define the STIRAP pulse area as $\mathcal{A} = \int_{-\infty}^{\infty} dt \sqrt{\Omega_{01}^2(t) + \Omega_{12}^2(t)}$ which is a measure of adiabaticity of the STIRAP process. In Figure 5a we show the population of state $|2\rangle$ as a function of the area of the counterdiabatic pulse and phase. We can also examine the dependence of the population p_2 on the STIRAP area \mathcal{A} , while keeping the counterdiabatic pulse area \mathcal{A}_{02} constant, see 5b. As expected from the previous gauge-invariance considerations and the use of a two-photon transition $|0\rangle \rightarrow |2\rangle$,

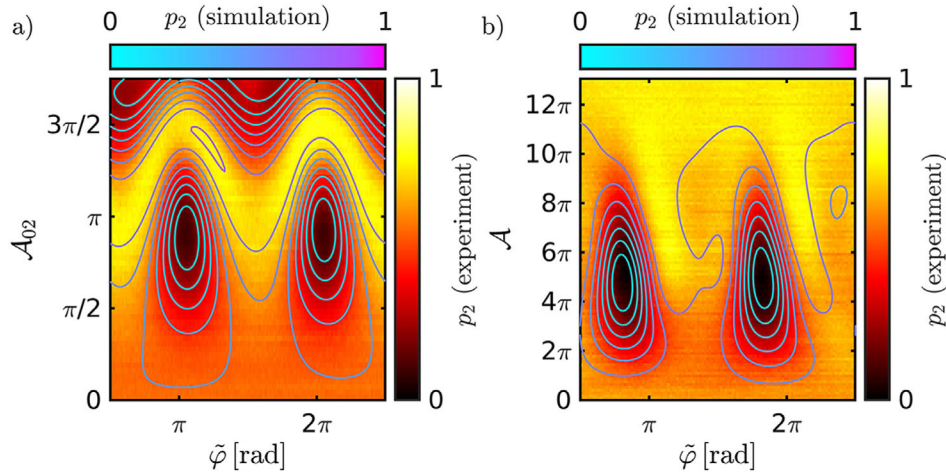


Figure 5. Observation of broken time-reversal symmetry, with experimental data shown as a continuum and the simulations as contour plots. We measure the transferred population as a function of the gauge-invariant phase Φ (controlled experimentally via the phase $\tilde{\varphi}$) at increasing values of the a) two-photon pulse area \mathcal{A}_{02} and b) STIRAP area \mathcal{A} . The experimental parameters were (a) $t_s = -61$ ns, $\sigma = 25$ ns, $\Omega_{01}/(2\pi) = 44$ MHz, $\Omega_{12}/(2\pi) = 36.8$ MHz, $\mathcal{A} = 5.5\pi$ and (b) $t_s = -37.5$ ns $\sigma = 25$ ns, and $\mathcal{A}_{02} = 0.81\pi$. The transition into the regime of broken time-reversal symmetry (corresponding to nonreciprocity in the spin system) is seen through the gradual emergence of Φ -dependence as (a) \mathcal{A}_{02} or (b) \mathcal{A} is increased.

the transfer is π -periodic in $\tilde{\varphi}$. One notices however small deviations from perfect π -periodicity especially in Figure 5b, reflecting the limitations of the two-photon approximation.

We further observe the main features of broken time-reversal symmetry: when both the STIRAP process and the counteradiabatic fields are on, the transfer is in general not symmetric under the transformation $\tilde{\varphi} \rightarrow -\tilde{\varphi} - (n+1)\pi$. The plots also show that if either one of the couplings is turned off, time-symmetry is restored. For example, in Figure 5a there is no phase dependence for $\mathcal{A}_{02} = 0$. Similarly, from Figure 5b we notice the absence of phase dependence for $\mathcal{A} = 0$, as expected when only the two-photon pulse is applied, while in the other extreme case, at large values $\mathcal{A} > 12\pi$, STIRAP dominates and the phase dependence becomes again weaker. In general, these patterns of transfer are complicated but they are reproduced very well by the numerical modeling of the total Hamiltonian (contour plots). For the ideal case of unitary evolution under $H_\Phi(t)$, the maximum transfer should occur at $\mathcal{A}_{02} = \pi$ (which follows immediately by using $\Omega_{02}(t) = 2\dot{\Theta}(t)$) and at $-2\tilde{\varphi} - \pi = \Phi = -\pi/2 + 2n\pi$ (or $\tilde{\varphi} \approx 3\pi/4 + n\pi$). However, in general the presence of the Hamiltonian H_{acStark} shifts these optimal phases and areas to other values (see Section 2, Supporting Information), depending on the specific parameters of the pulses. Still, the values of the measured optimal phases are reproduced quite well by the numerics, typically within 0.09π . In these regions of optimal transfer, the population on state $|2\rangle$ exceeds 0.9.

This experiment also shows, as emphasized in ref. [17], that an intimate connection exists between gauge invariance and time symmetry, which experimentally amounts to the fact that time-reversal symmetry is fully controlled by only one parameter, the gauge-invariant phase Φ .

4.3. Currents and Chirality

For transport phenomena in spin chains, the measurement and analysis of the currents provide important insights into

the dynamics. Much attention has been given so far to the case where the currents exhibit a circular flow, which can be made clockwise or anticlockwise by changes in the gauge-invariant phase.^[18,19] Here we will show that the analysis of currents give important insights into the mechanism by which the number of excitations transferred from one site to another is maximized by adiabatic processes.

To start with, let us calculate the time-dependent currents in a dark state. Using Equation (12) we find

$$\langle D(t) | I_{0 \rightarrow 2} | D(t) \rangle = \frac{1}{2} \Omega_{02}(t) \sin 2\Theta(t) \sin \phi_{02} \quad (29)$$

and

$$\langle D(t) | I_{0 \rightarrow 1} | D(t) \rangle = \langle D(t) | I_{1 \rightarrow 2} | D(t) \rangle = 0 \quad (30)$$

We notice that current $I_{0 \rightarrow 2}$ depends not only on Ω_{02} , as expected, but also on the mixing angle $\Theta(t)$. Clearly for equal-strength STIRAP pulses $\Omega_{01} = \Omega_{12}$ the maximum current is realized in the middle of the protocol, that is, at $t = t_s/2$. The magnitude of the current is modulated by the $\sin \phi_{02}$ factor. For $\phi_{02} = \pi/2$ (or $\Phi = -\pi/2$) we obtain a maximum current

$$\langle D(t) | I_{0 \rightarrow 2}^{\text{max}} | D(t) \rangle = \frac{1}{2} \Omega_{02}(t) \sin 2\Theta(t) \quad (31)$$

in the direction of increasing the population on the state $|2\rangle$. For $\phi_{02} = -\pi/2$ (or $\Phi = \pi/2$) the current would flow in the opposite direction: the transfer realized by STIRAP is undone by the two-photon pulse. The fact that the averages of $I_{0 \rightarrow 1}$ and $I_{1 \rightarrow 0}$ on the dark state are zero reflects the fact that the state $|1\rangle$ is not populated. The result has a paradoxical flavor, since a quanta is transferred along a trajectory without apparently going through the intermediate positions, which leads to infinite Bohmian velocities at those positions.^[84]

Let us examine now the time-derivative of the population $p_2(t) = \sin^2 \Theta(t)$; we find

$$\dot{p}_2(t) = \dot{\Theta}(t) \sin 2\Theta(t). \quad (32)$$

We can immediately compare Equations (29) and (30) with Equation (32). To have consistency between these results, we need to impose the condition $\Omega_{02}(t) = 2\dot{\Theta}(t)$ and $\phi_{02} = \pi/2$. These are precisely the requirements of superadiabatic driving.

Next, we give a more precise account of the intuition that saSTIRAP can be seen as a constructive interference effect between two paths, one corresponding to the STIRAP process and the other to the two-photon process. This argument illustrates surprisingly well why a purely imaginary value for the 0–2 driving is necessary.

Let us consider the case $\mathcal{A} = 0$. Since the state $|1\rangle$ is not populated, let us consider the two-photon process with Hamiltonian

$$H_{02} = \frac{\hbar}{2} \Omega_{02} \hat{\mathbf{n}}_{\Phi} \cdot \mathbf{\Lambda}_{02} \quad (33)$$

where $\hat{\mathbf{n}}_{\Phi} = (\cos \Phi, \sin \Phi)$ is a unit vector in the plane xOy and $\mathbf{\Lambda}_{02} = (\Lambda_{02}^s, \Lambda_{02}^a)$ is the vector formed by the symmetric and anti-symmetric Gell–Mann matrices. In this subspace the evolution operator is

$$U(t) = e^{-\frac{i}{\hbar} \int_{-\infty}^t d\tau H_{02}(\tau)} = e^{-\frac{i}{2} \int_{-\infty}^t d\tau \Omega_{02}(\tau) \hat{\mathbf{n}}_{\Phi} \cdot \mathbf{\Lambda}_{02}}. \quad (34)$$

Now, the components of $\mathbf{\Lambda}_{02}$ are essentially Pauli matrices in the 0–2 subspace (and all the other matrix elements are zero), therefore we can use a familiar formula for the exponential of Pauli matrices.

$$e^{i\mathbf{n}_{\Phi} \cdot \mathbf{\Lambda}_{02}} = \cos n + i\hat{\mathbf{n}}_{\Phi} \cdot \mathbf{\Lambda}_{02} \sin n, \quad (35)$$

with $n = -\frac{1}{2} \int_{-\infty}^t d\tau \Omega_{02}(\tau)$ and $\mathbf{n}_{\Phi} = n\hat{\mathbf{n}}_{\Phi}$, resulting in

$$U(t) = \cos \left(\frac{1}{2} \int_{-\infty}^t d\tau \Omega_{02}(\tau) \right) - i\hat{\mathbf{n}}_{\Phi} \cdot \mathbf{\Lambda}_{02} \sin \left(\frac{1}{2} \int_{-\infty}^t d\tau \Omega_{02}(\tau) \right) \quad (36)$$

Since $\Omega_{02}(t) = 2\dot{\Theta}(t)$, the state at any time is obtained as

$$|0\rangle \rightarrow U(t)|0\rangle = \cos \Theta(t)|0\rangle + e^{i(\Phi-\pi/2)} \sin \Theta(t)|2\rangle \quad (37)$$

It is instructive to see that this state coincides with the dark state precisely for $\Phi = -\pi/2$ as expected.

Now, for a π pulse from $t = -\infty$ to $t = \infty$ we have $\int_{-\infty}^{\infty} d\tau \Omega_{02}(\tau) = \pi$, resulting in

$$U_{\pi} = -i(\cos \Phi \Lambda_{02}^s + \sin \Phi \Lambda_{02}^a) \quad (38)$$

When applied to the initial state $|0\rangle$, this leads to

$$U_{\pi}|0\rangle = (-i \cos \Phi + \sin \Phi)|2\rangle \quad (39)$$

Suppose now that $\Phi = -\pi/2$ (up to integer multiples of 2π). This means that $U_{\pi}|0\rangle = -|2\rangle$. The same sign is obtained from

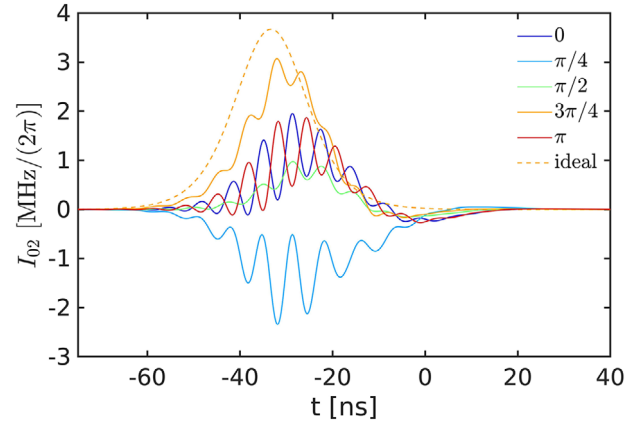


Figure 6. The averaged 0–2 current $\langle I_{02} \rangle$ at different values of $\tilde{\varphi}$. The parameters are the same as in Figure 5a for a counterdiabatic pulse area $\mathcal{A}_{02} = \pi$.

the STIRAP path, $|0\rangle \xrightarrow{\text{STIRAP}} -|2\rangle$, therefore we expect that these paths will interfere constructively. Conversely, if $\Phi = \pi/2$ (up to integer multiples of 2π), we expect destructive interference, since $U_{\pi}|0\rangle = +|2\rangle$. This is precisely what is observed in the experiment. That is, the dynamics along the STIRAP path occurs in the $\{|0\rangle, |2\rangle\}$ subspace.

In the experiments with the three-level simulator, the currents can be obtained by calculating the averages of the operators Equation (12) on the state extracted from experimental data. In **Figure 6** we present the current $\langle I_{02} \rangle$ at a few values of $\tilde{\varphi}$ for $\mathcal{A}_{02} = \pi$ and with the rest of the parameters as in Figure 5a. In general, the features we observe are consistent with the idealized model above; in addition, oscillations are present in the currents due to the ac Stark shift. At $\tilde{\varphi} = 3\pi/4 + n\pi$ we obtain a relatively large positive current. The envelope of this current matches well with the ideal-case analytical expression Equation (31), plotted with dotted line. As we depart from this optimal transfer point, the current becomes more oscillatory and smaller in value. It can even have negative values for points in the regions of minimal population transfer, as shown in Figure 6 for $\tilde{\varphi} = \pi/4$, signaling the transfer of population backward to state $|0\rangle$. Note also that the points $\pi/4$ and $3\pi/4$ are related by the time-reversal relation $\tilde{\varphi}' = -\tilde{\varphi} - (n+1)\pi$; thus, as expected, the currents show conclusively the signature of broken time-reversal symmetry. Finally, let us notice that the dark state in STIRAP and saSTIRAP involves superpositions of states with various chiralities. However, the average of the chirality operator on this state is zero

$$\langle D(t) | C_z | D(t) \rangle = 0 \quad (40)$$

reflecting the connection between chirality and asymmetry, namely the fact that the chirality is expressed in terms of only asymmetric Gell–Mann matrices Equation (13). In this sense, increasing \mathcal{A} in Figure 5b also results in a change of chirality. For $\mathcal{A} = 0$ we have

$$\langle 0 | U^\dagger(t) C_z U(t) | 0 \rangle = \frac{\sqrt{3}}{3} \cos \Phi \sin 2\Theta(t) \quad (41)$$

which is zero only at the beginning and at the end of the process ($\Theta = 0, \pi/2$) if $\Phi \neq \pm\pi/2$.

This is easy to understand in the Bloch-sphere picture for the subspace $\{|0\rangle, |2\rangle\}$. There, the dark state moves from the North pole to the South pole in the $z - O - x$ plane, while the chirality becomes the Pauli- y operator. The average value of the y -axis projection will be therefore zero at any time for the dark state.

5. Conclusions

We have employed a transmon superconducting circuit in the loop driving (Δ -driving) configuration as a simulator for a spin chain with XX and Dzyaloshinskii–Moryia couplings and subjected to time-dependent inhomogeneous broadening. We demonstrate that transport can be realized efficiently under the condition of superadiabaticity. We put in evidence the phenomenon of gauge invariance and we observe the manifestation of broken time-reversal symmetry. Finally, we extract the currents and show that the superadiabaticity condition leads to a maximum positive current flowing between the initial state and the target state.

Supporting Information

Supporting Information is available from the Wiley Online Library or from the author.

Acknowledgements

The authors are grateful to Sergey Danilin for sample preparation and assistance with the cryogenics and the measurements and to Shruti Dogra and Pieter W. Claeys for useful comments on the manuscript. This work used the cryogenic facilities of the Low Temperature Laboratory at Aalto University. The authors are grateful for financial support from FQXi, Väisälä Foundation, EU project 862644-QUARTET, and the Academy of Finland through project nos. 263457, 250280, and 328193. The authors also acknowledge the “Finnish Center of Excellence in Quantum Technology” of the Academy of Finland (project no. 312296).

Conflict of Interest

The authors declare no conflict of interest.

Keywords

broken time-reversal symmetry, quantum simulation, spin lattices, superadiabatic, superconducting quantum circuits

Received: October 30, 2019

Revised: January 20, 2020

Published online: February 5, 2020

[1] R. P. Feynman, *Int. J. Theor. Phys.* **1982**, 21, 467.

[2] S. Lloyd, *Science* **1996**, 273, 1073.

- [3] M. A. Nielsen, I. L. Chuang, *Quantum Computing and Quantum Information*, Cambridge University Press, Cambridge **2000**.
- [4] Y. Salathé, M. Mondal, M. Oppliger, J. Heinsoo, P. Kurpiers, A. Potočnik, A. Mezzacapo, U. Las Heras, L. Lamata, E. Solano, S. Filip, A. Wallraff, *Phys. Rev. X* **2015**, 5, 021027.
- [5] R. Barends, A. Shabani, L. Lamata, J. Kelly, A. Mezzacapo, U. L. Heras, R. Babbush, A. G. Fowler, B. Campbell, Y. Chen, Z. Chen, B. Chiaro, A. Dunsworth, E. Jeffrey, E. Lucero, A. Megrant, J. Y. Mutus, M. Neeley, C. Neill, P. J. J. O'Malley, C. Quintana, P. Roushan, D. Sank, A. Vainsencher, J. Wenner, T. C. White, E. Solano, H. Neven, J. Martinis, *Nature* **2016**, 534, 222.
- [6] G. S. Paraoanu, *J. Low Temp. Phys.* **2014**, 175, 633.
- [7] M. Neeley, M. Ansmann, R. C. Bialczak, M. Hofheinz, E. Lucero, A. D. O'Connell, D. Sank, H. Wang, J. Wenner, A. N. Cleland, M. R. Geller, J. M. Martinis, *Science* **2009**, 325, 722.
- [8] E. Svetitsky, H. Suchowski, R. Resh, Y. Shalibo, J. M. Martinis, N. Katz, *Nat. Commun.* **2014**, 5, 5617.
- [9] J. Li, M. Silveri, K. S. Kumar, J.-M. Pirkkalainen, A. Vepsäläinen, W. Chien, J. Tuorila, M. Sillanpää, P. Hakonen, E. Thuneberg, G. S. Paraoanu, *Nat. Commun.* **2013**, 4, 1420.
- [10] I. E. Dzialoshinskii, *J. Exp. Theoret. Phys.* **1957**, 32, 1547.
- [11] T. Moriya, *Phys. Rev. Lett.* **1960**, 4, 228.
- [12] Z. Huang, H. Situ, C. Zhang, *Int. J. Theor. Phys.* **2017**, 56, 2178.
- [13] M. Kargarian, R. Jafari, A. Langari, *Phys. Rev. A* **2009**, 79, 042319.
- [14] F.-W. Ma, S.-X. Liu, X.-M. Kong, *Phys. Rev. A* **2011**, 84, 042302.
- [15] T. Farajollahpour, S. A. Jafari, *Phys. Rev. B* **2018**, 98, 085136.
- [16] X. ke Song, T. Wu, S. Xu, J. He, L. Ye, *Ann. Phys.* **2014**, 349, 220.
- [17] J. Koch, A. A. Houck, K. L. Hur, S. M. Girvin, *Phys. Rev. A* **2010**, 82, 043811.
- [18] P. Roushan, C. Neill, A. Megrant, Y. Chen, R. Babbush, R. Barends, B. Campbell, Z. Chen, B. Chiaro, A. Dunsworth, A. Fowler, E. Jeffrey, J. Kelly, E. Lucero, J. Mutus, P. O'Malley, M. Neeley, C. Quintana, D. Sank, A. Vainsencher, J. Wenner, T. White, E. Kapit, H. Neven, J. Martinis, *Nat. Phys.* **2017**, 13, 146.
- [19] D.-W. Wang, C. Song, W. Feng, H. Cai, D. Xu, H. Deng, D. Zheng, X. Zhu, H. Wang, S. Zhu, M. O. Scully, *Nat. Phys.* **2019**, 15, 382.
- [20] L. M. de Lépinay, E. Damskägg, C. F. Ockeloen-Korppi, M. A. Sillanpää, *Phys. Rev. Appl.* **2019**, 11, 034027.
- [21] G. Petersen, F. Lecocq, K. Cicak, R. W. Simmonds, J. Aumentado, J. D. Teufel, *Phys. Rev. X* **2017**, 7, 031001.
- [22] N. R. Bernier, L. D. Tóth, A. Koottandavida, M. A. Ioannou, D. Malz, A. Nunnenkamp, A. K. Feofanov, T. J. Kippenberg, *Nat. Commun.* **2017**, 8, 604.
- [23] S. Barzanjeh, M. Wulf, M. Peruzzo, M. Kalaei, P. B. Dieterle, O. Painter, J. Fink, *Nat. Commun.* **2017**, 8, 953.
- [24] M. Aidelsburger, M. Atala, M. Lohse, J. T. Barreiro, B. Paredes, I. Bloch, *Phys. Rev. Lett.* **2013**, 111, 185301.
- [25] I. I. Rabi, *Phys. Rev.* **1937**, 51, 652.
- [26] M. Born, V. Fock, *Z. Phys.* **1928**, 51, 165.
- [27] R. Menchon-Enrich, A. Benseny, V. Ahufinger, A. D. Greentree, T. Busch, J. Mompart, *Rep. Prog. Phys.* **2016**, 79, 074401.
- [28] S. Oh, Y.-P. Shim, J. Fei, M. Friesen, X. Hu, *Phys. Rev. A* **2013**, 87, 022332.
- [29] A. D. Greentree, J. H. Cole, A. R. Hamilton, L. C. L. Hollenberg, *Phys. Rev. B* **2004**, 70, 235317.
- [30] C. J. Bradley, M. Rab, A. D. Greentree, A. M. Martin, *Phys. Rev. A* **2012**, 85, 053609.
- [31] R. Menchon-Enrich, S. McEndoo, T. Busch, V. Ahufinger, J. Mompart, *Phys. Rev. A* **2014**, 89, 053611.
- [32] S. Longhi, *Ann. Phys.* **2014**, 348, 161.
- [33] K. Bergmann, H.-C. Nägerl, C. Panda, G. Gabrielse, E. Miloglyadov, M. Quack, G. Seyfang, G. Wichmann, S. Ospelkaus, A. Kuhn, S. Longhi, A. Szameit, M. Drewsen, W. K. Hensinger, S. Weidt, T. Halfmann, H. Wang, G. S. Paraoanu, N. V. Vitanov, J. Mompart, T. Busch,

- T. J. Barnum, D. D. Grimes, R. W. Field, M. G. Raizen, E. Narevicius, M. Auzinsh, D. Budker, A. P'alfy, C. H. Keitel, *J. Phys. B: At. Mol. Opt. Phys.* **2019**, *52*, 202001.
- [34] M. V. Berry, *J. Phys. A: Math. Theor.* **2009**, *42*, 365303.
- [35] A. Emmanouilidou, X.-G. Zhao, P. Ao, Q. Niu, *Phys. Rev. Lett.* **2000**, *85*, 1626.
- [36] M. Demirplak, S. Rice, *J. Phys. Chem. A* **2003**, *107*, 9937.
- [37] M. Demirplak, S. Rice, *J. Phys. Chem. B* **2005**, *109*, 6838.
- [38] M. Demirplak, S. A. Rice, *J. Chem. Phys.* **2008**, *129*, 154111.
- [39] E. Torrontegui, S. Ibáñez, S. Martínez-Garaot, M. Modugno, A. del Campo, D. Guéry-Odelin, A. Ruschhaupt, X. Chen, J. G. Muga, *Advances in Atomic, Molecular, and Optical Physics*, Academic Press, San Diego, CA **2013**.
- [40] A. Benseny, A. Kiely, Y. Zhang, T. Busch, A. Ruschhaupt, *EPJ Quantum Technol.* **2017**, *4*, 3.
- [41] J. Koch, T. M. Yu, J. Gambetta, A. A. Houck, D. I. Schuster, J. Majer, A. Blais, M. H. Devoret, S. M. Girvin, R. J. Schoelkopf, *Phys. Rev. A* **2007**, *76*, 042319.
- [42] A. Wallraff, D. I. Schuster, A. Blais, L. Frunzio, R.-S. Huang, J. Majer, S. Kumar, S. M. Girvin, R. J. Schoelkopf, *Nature* **2004**, *431*, 162.
- [43] C. E. Carroll, F. T. Hioe, *J. Opt. Soc. Am. B* **1988**, *5*, 1335.
- [44] M. Fleischhauer, R. Unanyan, B. W. Shore, K. Bergmann, *Phys. Rev. A* **1999**, *59*, 3751.
- [45] R. Unanyan, L. Yatsenko, K. Bergmann, B. Shore, *Opt. Commun.* **1997**, *139*, 48.
- [46] T. J. Pope, J. Rajendran, A. Ridolfo, E. Paladino, F. M. Pellegrino, G. Falci, *arXiv:1908.01145*, **2019**.
- [47] P. G. Di Stefano, E. Paladino, T. J. Pope, G. Falci, *Phys. Rev. A* **2016**, *93*, 051801.
- [48] A. Vepsäläinen, S. Danilin, G. S. Paraoanu, *Quantum Sci. Technol.* **2018**, *3*, 024006.
- [49] A. Vepsäläinen, S. Danilin, G. S. Paraoanu, *Sci. Adv.* **2019**, *5*, eaau5999.
- [50] N. Aharon, I. Cohen, F. Jelezko, A. Retzker, *New J. Phys.* **2016**, *18*, 123012.
- [51] N. Goldman, G. Juzeliunas, P. Öhberg, I. B. Spielman, *Rep. Prog. Phys.* **2014**, *77*, 126401.
- [52] J. Dalibard, F. Gerbier, G. Juzeliunas, P. Öhberg, *Rev. Mod. Phys.* **2011**, *83*, 1523.
- [53] D. Banerjee, M. Bögli, M. Dalmonte, E. Rico, P. Stebler, U.-J. Wiese, P. Zoller, *Phys. Rev. Lett.* **2013**, *110*, 125303.
- [54] R. J. Cookz, B. W. Shore, *Phys. Rev. A* **1979**, *20*, 539.
- [55] F. T. Hioe, *J. Opt. Soc. Am. B* **1987**, *4*, 1327.
- [56] E. Farhi, J. Goldstone, S. Gutmann, J. Lapan, A. Lundgren, D. Preda, *Science* **2001**, *292*, 472.
- [57] A. Das, B. K. Chakrabarti, *Rev. Mod. Phys.* **2008**, *80*, 1061.
- [58] M. W. Johnson, M. H. S. Amin, S. Gildert, T. Lanting, F. Hamze, N. Dickson, R. Harris, A. J. Berkley, J. Johansson, P. Bunyk, E. M. Chapple, C. Enderud, J. P. Hilton, K. Karimi, E. Ladizinsky, N. Ladizinsky, T. Oh, I. Perminov, C. Rich, M. C. Thom, E. Tolkacheva, C. J. S. Truncik, S. Uchaikin, J. Wang, B. Wilson, G. Rose, *Nature* **2011**, *473*, 194.
- [59] E. Sjöqvist, D. M. Tong, L. M. Andersson, B. Hessmo, M. Johansson, K. Singh, *New J. Phys.* **2012**, *14*, 103035.
- [60] P. Zanardi, M. Rasetti, *Phys. Lett. A* **1999**, *264*, 94.
- [61] A. A. Abdumalikov, J. M. Fink, K. Juliusson, M. Pechal, S. Berger, A. Wallraff, S. Filipp, *Nature* **2013**, *496*, 482.
- [62] S. Boixo, T. F. Rønnow, S. V. Isakov, Z. Wang, D. Wecker, D. A. Lidar, J. M. Martinis, T. Matthias, *Nat. Phys.* **2014**, *10*, 218.
- [63] L. Chotorlishvili, M. Azimi, S. Stagraczynski, Z. Toklikishvili, M. Schüler, J. Berakdar, *arXiv:1608.01977*, **2016**.
- [64] P. Salamon, K. H. Hoffmann, Y. Rezek, R. Kosloff, *Phys. Chem. Chem. Phys.* **2009**, *11*, 1027.
- [65] Y. Rezek, P. Salamon, K. H. Hoffmann, R. Kosloff, *Europhys. Lett.* **2009**, *85*, 30008.
- [66] X. Chen, J. G. Muga, *Phys. Rev. A* **2010**, *82*, 053403.
- [67] P. W. Claeys, M. Pandey, D. Sels, A. Polkovnikov, *arXiv:1904.03209v1*, **2019**.
- [68] Y. Ban, X. Chen, S. Kohler, G. Platero, *arXiv:1904.05694v1*, **2019**.
- [69] K. Groenland, *SciPost Phys.* **2019**, *6*, 11.
- [70] L. Lima, *Physica C* **2018**, *549*, 147.
- [71] M. Sentef, M. Kollar, A. P. Kampf, *Phys. Rev. B* **2007**, *75*, 214403.
- [72] J. K. Pachos, M. B. Plenio, *Phys. Rev. Lett.* **2004**, *93*, 056402.
- [73] T. Graß, C. Muschik, A. Celi, R. W. Chhajlany, M. Lewenstein, *Phys. Rev. A* **2015**, *91*, 063612.
- [74] X. G. Wen, F. Wilczek, A. Zee, *Phys. Rev. B* **1989**, *39*, 11413.
- [75] X. Chen, I. Lizuain, A. Ruschhaupt, D. Guéry-Odelin, J. G. Muga, *Phys. Rev. Lett.* **2010**, *105*, 123003.
- [76] L. Giannelli, E. Arimondo, *Phys. Rev. A* **2014**, *89*, 033419.
- [77] M. Kolodrubetz, D. Sels, P. Mehta, A. Polkovnikov, *Phys. Rep.* **2017**, *697*, 1.
- [78] R. Bianchetti, S. Filipp, M. Baur, J. M. Fink, C. Lang, L. Steffen, M. Boissonneault, A. Blais, A. Wallraff, *Phys. Rev. Lett.* **2010**, *105*, 223601.
- [79] A. A. Abdumalikov, O. Astafiev, A. M. Zagoskin, Y. A. Pashkin, Y. Nakamura, J. S. Tsai, *Phys. Rev. Lett.* **2010**, *104*, 193601.
- [80] J. Li, G. S. Paraoanu, K. Cicak, F. Altomare, J. I. Park, R. W. Simmonds, M. A. Sillanpää, P. J. Hakonen, *Phys. Rev. B* **2011**, *84*, 104527.
- [81] K. S. Kumar, A. Vepsäläinen, S. Danilin, G. S. Paraoanu, *Nat. Commun.* **2016**, *7*, 10628.
- [82] D. F. James, J. Jerke, *Can. J. Phys.* **2007**, *85*, 625.
- [83] R. Peierls, *Z. Phys.* **1933**, *80*, 763.
- [84] A. Benseny, J. Bagudà, X. Oriols, J. Mompert, *Phys. Rev. A* **2012**, *85*, 053619.
- [85] A. Vepsäläinen, S. Danilin, E. Paladino, G. Falci, G. S. Paraoanu, *Photonics* **2016**, *3*, 62.